Enhancing Corrosion Resistance and Mechanical Strength of 3D-Printed Iron Polylactic Acid for Marine Applications via Laser Surface Texturing

Mohammad Rezayat, Mojtaba Karamimoghadam, Mohammadreza Lalegani Dezaki, Ali Zolfagharian, Giuseppe Casalino, Antonio Mateo, and Mahdi Bodaghi*

The corrosion susceptibility and limited mechanical properties of 3D-printed iron polylactic acid (Ir-PLA) pose challenges to its application in demanding environments, particularly in marine settings. This study investigates the potential of laser surface texturing (LST) to mitigate corrosion and enhance the mechanical performance of Ir-PLA 3D printed by fused deposition modeling for saline conditions, in which the fabricated materials are exposed to the seawater environment. A design of experiment approach is employed to systematically evaluate the effects of laser power and scanning speed on surface roughness, contact angle, and tensile test as mechanical properties. Results demonstrate that LST can significantly improve the corrosion resistance of Ir-PLA, with optimal parameters reducing surface degradation by up to 80%. Furthermore, the laser-treated samples exhibit a substantial increase in mechanical properties, with tensile strength improving by an average of 25% and ductility increasing by 15%, attributed to the microstructural modifications and patterned surface texture induced by the LST process. The findings highlight the potential of LST as a powerful tool for tailoring the surface characteristics and mechanical behavior of 3D-printed Ir-PLA in the seawater-simulated environment, opening new possibilities for its use in marine applications.

1. Introduction

The marine environment, characterized by its high salinity, constant exposure to moisture, and the presence of various corrosive agents, poses a significant challenge to the longevity and structural integrity of materials used in maritime applications.[1–3] The relentless assault of seawater, coupled with mechanical stresses and biofouling, accelerates the degradation of traditional metallic components, necessitating frequent maintenance, repairs, and replacements. This not only incurs substantial economic costs but also raises concerns about the safety and reliability of marine structures and vessels.[4,5] The maritime industry is, therefore, in constant pursuit of innovative materials and technologies that can withstand harsh marine conditions while offering advantages such as lightweight construction,[6] ease of fabrication, and cost-effectiveness. The advent of additive manufacturing, commonly known as 3D printing, has revolutionized various industries, including the maritime sector,[7,8] by enabling the rapid and customizable production of complex geometries.[9–11] The ability to fabricate parts on demand, with minimal material waste and reduced lead times, has made 3D printing an attractive alternative to traditional manufacturing methods.[12,13] Among the various 3D printing materials, iron-infused polylactic acid (PLA) has emerged as a promising candidate for marine applications[14] due to its unique combination of properties.[15–18]

Iron PLA (Ir-PLA) is a composite material that incorporates iron particles within a PLA matrix. PLA, a biodegradable polymer derived from renewable resources such as corn starch or sugarcane, offers advantages such as low cost, ease of processing, and environmental friendliness.[18–20] Iron particles are added to PLA

M. Rezayat, A. Mateo
Center for Structural Integrity, Micromechanics, and Reliability of Materials (CIEFMA)-Department of Materials Science and Engineering
Universitat Politècnica de Catalunya-BarcelonaTECH
08019 Barcelona, Spain

The ORCID identification number(s) for the author(s) of this article can be found under https://doi.org/10.1002/adem.202402591.

M. Karamimoghadam, G. Casalino
Department of Mechanics, Mathematics and Management
Polytechnic University of Bari
Via Orabona 4, 70125 Bari, Italy

M. L. Dezaki, M. Bodaghi
Department of Engineering
School of Science and Technology
Nottingham Trent University
Nottingham NG11 8NS, UK
E-mail: mahdi.bodaghi@ntu.ac.uk

A. Zolfagharian
School of Engineering
Deakin University
Geelong, VIC 3216, Australia

filaments to create composite materials with unique properties. This enhances the filament's magnetic properties, making it useful for electronics and mechanical parts, while also giving prints a metallic appearance suitable for decorative or artistic applications. The increased density provides a heavier, more substantial feel, ideal for replicas or high-quality prototypes, and the material allows for postprocessing options like polishing, sanding, or rusting for creative effects. Additionally, iron improves thermal conductivity, useful in heat-related applications. However, using iron-filled PLA requires hardened steel nozzles due to its abrasive nature and precautions to prevent rusting in finished prints. The addition of iron particles enhances the mechanical strength, stiffness, and thermal stability of PLA, making it suitable for structural and functional applications.[21,22] Moreover, the presence of iron imparts magnetic properties to the material, opening up possibilities for applications in sensors, actuators, and electromagnetic shielding.[23] However, the inherent susceptibility of iron to corrosion in saline environments remains a significant challenge to the widespread adoption of Ir-PLA in marine applications. The presence of chloride ions in seawater accelerates the corrosion of iron, leading to the formation of rust and the degradation of the material's mechanical properties.[24,25] This necessitates the development of effective strategies to mitigate corrosion and enhance the durability of Ir-PLA in marine environments.

Laser surface texturing (LST) has emerged as a promising technique for modifying the surface properties of materials, including 3D-printed polymers.[26–28] LST involves the use of a focused laser beam to create micro- and nanoscale features on the surface of a material. These features can significantly alter the material's surface chemistry, morphology, and wettability, thereby influencing its interaction with the surrounding environment.[29–31] LST has been shown to improve various properties of materials like metals[32] and polymers,[33] such as adhesion, friction, wear resistance,[34] and corrosion resistance.[35,36] The patterned surface texture created by LST can also influence the wettability of the material, potentially reducing the contact area between the material and the corrosive medium, thereby hindering the corrosion process. Furthermore, LST can induce microstructural changes in the material, such as grain refinement or the formation of beneficial residual stresses, which can further enhance its mechanical properties[37] and corrosion resistance.[38–40] The application of LST to 3D-printed Ir-PLA composites presents significant opportunities for various industries, especially in harsh environments like the marine sector. LST enhances corrosion resistance, mechanical strength, and durability, making this material suitable for demanding applications. In the marine industry, LST-treated Ir-PLA can be utilized for lightweight and corrosion-resistant components such as boat hulls, propellers, and underwater structures, reducing corrosion from saltwater exposure and extending the lifespan of marine vessels while lowering maintenance costs. Underwater sensors and actuators could also benefit from the improved robustness and corrosion resistance.[11,41] In the oil and gas sector, where equipment faces corrosive conditions, LST-treated Ir-PLA components like pipes and valves would experience reduced degradation and enhanced durability, minimizing breakdowns and maintenance costs.[8] Additionally, this material can be employed in offshore wind turbines, improving longevity and reducing downtime in renewable energy systems. In aerospace, LST-treated Ir-PLA could serve in lightweight, corrosion-resistant structural components or protective coatings.[42–44] Furthermore, in the automotive industry, components such as brake pads and exhaust systems could leverage enhanced mechanical properties and corrosion resistance, leading to longer-lasting parts and decreased replacement frequency, even in marine animal implants like sensors.[45,46]

Several studies have investigated the use of LST to enhance properties of metals[35,47] and polymers,[48] improving wear resistance, adhesion, and hydrophobicity in metals, as well as surface roughness and mechanical strength in polymer composites.[49] However, most research has focused on metallic or polymer systems, overlooking metal-infused polymers in harsh environments. This study uniquely examines LST on 3D-printed Ir-PLA composites, addressing corrosion challenges from iron particles. While some studies on PLA composites exist,[6,50] this is the first to optimize LST parameters for marine applications, enhancing both corrosion resistance and mechanical strength.

This study investigates the potential of LST to mitigate corrosion and enhance the mechanical properties of Ir-PLA 3D printed by FDM for saline applications. The research focuses on optimizing the LST process parameters, namely laser power and scanning speed, to achieve desired surface characteristics and mechanical behavior. The effects of LST on the width of the laser track, surface roughness, contact angle, and mechanical properties of Ir-PLA are systematically investigated. The corrosion resistance of the laser-treated samples is evaluated in a simulated saline environment, and the underlying mechanisms responsible for the observed improvements are discussed. The ability to fabricate complex, lightweight, and corrosion-resistant components on demand could revolutionize the maritime industry, leading to more efficient, sustainable, and cost-effective solutions. Potential applications include boat hulls and propellers, underwater sensors and actuators, marine structures, and even biomedical implants for marine organisms. In addition to its potential benefits for the maritime industry, this research also contributes to the broader field of additive manufacturing and materials science. The understanding gained from this study on the effects of LST on the properties of Ir-PLA can be extended to other 3D printed materials and applications, further expanding the possibilities of additive manufacturing for creating advanced materials with tailored properties.

2. Experimental Section

2.1. Material (Filament)

The application of fused deposition modeling (FDM) can be used to create products with a variety of material qualities and multifunctional features by utilizing a range of thermoplastic filaments that are now available and may integrate functional additive particles. Through deliberate alteration of the print at specific spots, these qualities can be customized throughout the print. This work uses iron-filled PLA from Proto-Pasta (Vancouver, WA). Iron powder with a particle size of 250 μm is combined with PLA-based material. Protopasta Company produces 2.85 mm PLA filament that has been loaded with 15 wt%

iron. This oxidizable filament is made of ferromagnet material, which behaves like pure iron when exposed to a magnetic field. The iron particles are encased in plastic, which keeps them stable and matte when printed. However, they can be oxidized to produce rusted decorative pieces if required. When compared to regular PLA, this filament is more abrasive. To increase the length of service intervals when printing with this filament, it is better to use a nozzle that is more resistant to wear or one with a larger diameter. This design space is examined using the surface quality, mechanical properties, and LST.
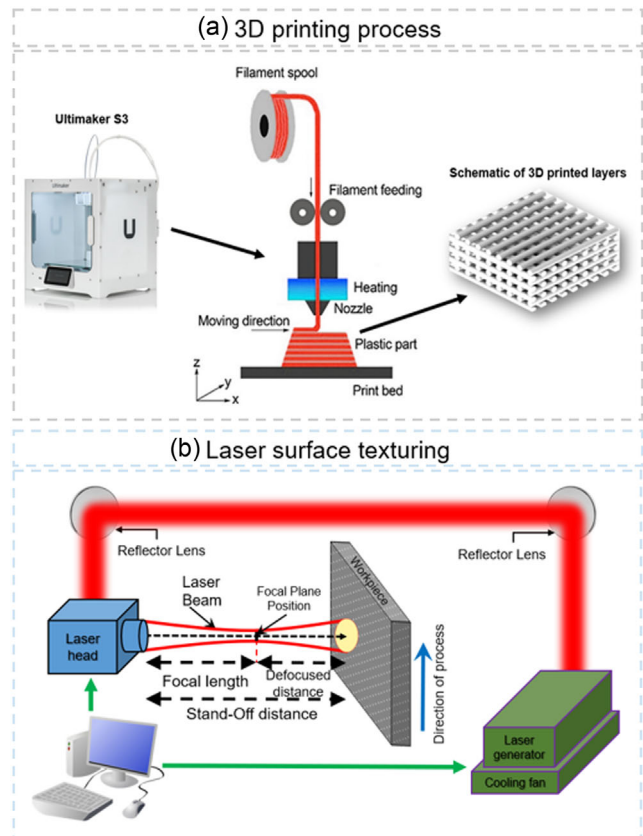
2.2. Design of Experiments and 3D Printing and Laser Surface Texturing

The experimental design employed in this study was a 3^2 factorial design, which systematically investigated the effects of two input variables (factors)—laser power and scanning speed—on three output variables (responses)—width of the laser track, surface roughness (Ra), and contact angle. The three levels for laser power were 40, 50, and 60 W, while the three levels for scanning speed were 1.2, 3.6, and 6 mm s^{-1} (see **Table 1**). The data collected from these experiments were then analyzed using Design-Expert Software (Minneapolis, MN) to develop mathematical models and optimize the process parameters for desired outcomes. The 3^2 factorial design allowed for the efficient exploration of the parameter space and the identification of significant factors and interactions influencing the responses. The use of statistical analysis, such as analysis of variance (ANOVA), further enabled the validation of the models and the assessment of the relative importance of the factors. The optimization process, based on the defined constraints and goals, led to the identification of the optimal laser power and scanning speed settings for achieving the desired surface characteristics and mechanical behavior of the Ir-PLA samples.

Structures and designs created with SolidWorks software. Specimens were designed and created with dimensions of 150 mm for length, 150 mm for width, and 2 mm for thickness. A two-nozzle, 0.6 mm Ultimaker S3 FDM-style 3D printer was used to produce every structure in this investigation (see **Figure 1**a). The Computer-Aided Design (CAD) file is sliced and converted to gcode files using the Cura software. The following printing settings are necessary to ensure smooth nozzle extrusion of 2.85 mm Ir-PLA filament. For 3D printing with Ir-PLA (details in **Table 2**), the first layer was printed at a speed of 15 mm s^{-1}, while the remaining layers were printed at 70 mm s^{-1}. The nozzle temperature was set at 205 °C, with the highest temperature at 220 °C used for the first layer to improve adhesion. A standard or wear-resistant nozzle with a preferred diameter of 0.6 mm was utilized. The layer thickness was maintained at 0.2 mm, and the bed temperature was kept at 60 °C.

Figure 1. Schematic diagrams for a) 3D printing FDM process by single filament and b) LST process setup with scanner.

All the samples had the same 45° raster angle, linear infill pattern, 100% infill density, 0° build orientation, and no support structure. The bed was prepared with Elmer's purple disappearing glue stick or another suitable PLA surface preparation.

The LST process in this study was conducted using a pulsed Nd:YLF glass laser (Explorer-One-349-120, Spectra-Physics) with a wavelength of 349 nm. The laser was operated in pulsed mode with a maximum peak power of 60 W and a maximum repetition rate of 1 KHz. The laser beam was focused onto the workpiece surface with a focal length of 80 mm, resulting in a spot size diameter of 145 μm. The experimental setup involved a stand-off distance of 150 mm between the workpiece surface and the nozzle, and the laser's focal plane was positioned 70 mm from the workpiece surface (see Figure 1b). A square-shaped pattern was chosen for the surface texture to ensure a homogeneous and uniform laser effect across the entire treated surface. The LST process was controlled using WeldMark software v12, with the laser beam oriented perpendicular to the target surface. The pattern consisted of vertical and horizontal tracks spaced 100 μm apart, and the pulse duration was set at 2 μs. The pulse energy, heat input, and laser spot overlap were calculated using Equation (1)–(3), respectively. The values for these parameters for each experimental run are presented in **Table 3**. The patterned surfaces were stored in a controlled laboratory environment for 45 days to allow for changes in contact angle and the

Table 1. Input variables and their corresponding design levels for the process parameters.

Variable	Symbol	Units	−1	0	1
Scanning speed	S	mm s^{-1}	1.2	3.6	6
Laser power	P	W	40	50	60

**ADVANCED
SCIENCE NEWS**

www.advancedsciencenews.com

**ADVANCED
ENGINEERING
MATERIALS**

www.aem-journal.com

Table 2. 3D printing parameters for Ir-PLA samples.

Parameter	Value	Description
Nozzle temperature	205 °C (first layer), 220 °C	Temperature used to extrude the Ir-PLA filament, with a higher initial layer temperature for adhesion.
Bed Temperature	60 °C	Maintained to ensure proper adhesion of the Ir-PLA filament during the printing process.
Layer thickness	0.2 mm	The thickness of each printed layer, contributing to surface quality and resolution.
Nozzle diameter	0.6 mm	A larger nozzle was used to accommodate the abrasive nature of Ir-PLA and ensure smooth extrusion.
Printing speed	15 mm s^{-1} (first layer), 70 mm s^{-1}	Speed of extrusion, with a slower speed for the first layer to enhance adhesion, and a faster speed for subsequent layers.
Infill density	100%	Ensures solid parts without voids, enhancing the mechanical strength of the printed components.
Raster angle	45°	Orientation of the print paths, contributing to the structural integrity of the printed parts.
Infill pattern	Linear	Chosen for its simplicity and effectiveness in ensuring uniform material distribution.
Build orientation	0°	The orientation of the build, with 0° being the default flat orientation for all samples.
Filament diameter	2.85 mm	Diameter of the Ir-PLA filament used in the 3D printing process.

Table 3. Configuration of experiments for laser processing.

Sample No.	Laser power [W]	Scanning speed [mm s^{-1}]	Pulse energy [µJ]	Heat input [KJ]	Laser spot overlap [%]
#1	40	1.2	80	31.6	93
#2	40	3.6	80	10.5	81
#3	40	6	80	6.3	68
#4	50	1.2	100	39.5	93
#5	50	3.6	100	13.1	81
#6	50	6	100	7.9	68
#7	60	1.2	120	47.5	93
#8	60	3.6	120	15.8	81
#9	60	6	120	9.5	68

potential attainment of a superhydrophobic state. The equation for calculating pulse energy is[51,52]

$$E = P \times \tau \tag{1}$$

where E is the pulse energy (in microjoules, µJ), P is the average power of the laser (in watts, W), and τ is the pulse duration (in seconds, s).[53]

$$Q = P \times \tau \times \eta \tag{2}$$

where Q is the heat input (in kilojoules, kJ), P is the average power of the laser (in watts, W), τ is the pulse duration (in seconds, s), and η is the efficiency of the process (0.85) (as a decimal).[53,54]

$$\text{Laser spot overlap} = \frac{\text{spot diameter} - \text{travel distance}}{\text{spot diameter}} \times 100\% \tag{3}$$
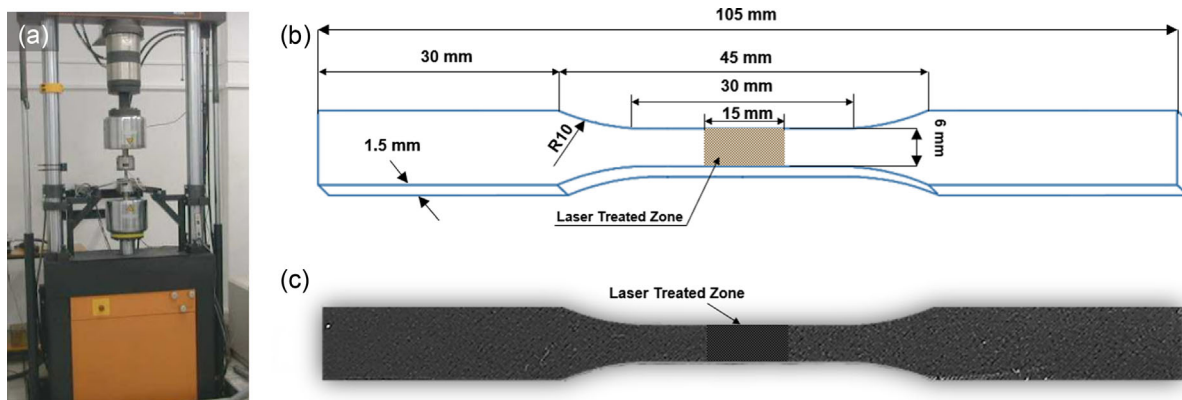
2.3. Tensile Test

The tensile tests were conducted using an INSTRON 8500 MODEL 1342 (see **Figure 2**a) machine, employing specimens designed in accordance with the ASTM E8M-96 standard,[55,56]

as illustrated in Figure 2b. The specimens were prepared with a laser-treated zone in the central part, measuring 15 mm in length, while the overall gauge length was 30 mm. It's important to note that both side of each specimen was subjected to LST (see Figure 2c). The tests were carried out at room temperature under ambient air conditions, with a consistent strain rate of 0.05 mm s^{-1}. To ensure statistical reliability, five specimens were tested for each condition (treated), allowing for the calculation of average values and their corresponding dispersion. In addition to the laser-treated specimens, untreated specimens were also tested to establish a baseline for comparison and evaluate the influence of LST on the mechanical response of the Ir-PLA material.

2.4. Corrosion Test

The corrosion resistance of the laser-textured Ir-PLA samples was evaluated using an immersion corrosion test, following the ASTM G31 standard.[57] The samples were submerged in a 3.5% sodium chloride (NaCl) solution, a standard medium for simulating marine environments, to assess their resistance to corrosion in a saline setting. The test likely involved measuring the weight loss of the samples due to corrosion over a specific period. The corrosion rate was then calculated and normalized to units of time, typically millimeters per year (mm year^{-1}) or mils per year (m year^{-1}). The lower the corrosion rate, the higher the corrosion resistance of the material. The specific duration of the immersion test was not explicitly detailed in the provided data; however, the text mentions that the patterned surfaces were stored in a controlled laboratory environment for 45 days before contact angle measurements. It's possible that this 45 day period also corresponds to the immersion time for the corrosion test. The volume of the saline solution would depend on the size and number of samples being tested, as well as the specific requirements of the ASTM G31 standard, which was likely followed for the corrosion rate calculations. The visual comparison of the corroded surfaces, as presented in the images in the results of this study, likely served as a qualitative assessment of the effectiveness of LST in enhancing the corrosion resistance of Ir-PLA.

Figure 2. a) INSTRON 8500 tensile test machine setup and b) schematic and c) actual photograph of tensile test specimen in this study in accordance with the ASTM E8M-96 standard.

2.5. Surface Characterization

Following the LST process, the samples were characterized to assess the impact of the treatment on their surface properties. The primary focus was on evaluating the morphological changes induced by LST, particularly the surface roughness and wettability. A LEXT OLS3100 (Tokyo, Japan) laser scanning confocal microscope (LSCM) was employed for the surface roughness determination. This advanced imaging technique facilitated the profiling of patterns post-LST and provided insights into surface geometry, enabling the evaluation of key roughness parameters. The LSCM utilizes a focused laser beam to capture precise height data from multiple points across the sample surface, generating a topographic map that intricately illustrates surface roughness. Five measurements were taken per sample at $20\times$ magnification, with a lateral resolution of $0.9\,\mu m$ and a vertical resolution of $50\,nm$. The analyzed area was $400 \times 400\,\mu m^2$. Corrections were applied to eliminate the general geometric shape and potential misfits resulting from measurements in order to level the profile. The surface wettability of the laser-textured surfaces was assessed by measuring the static water contact angles. A surface energy evaluation system from Advex Instruments (Brno, Czech Republic) was used for this purpose. To prevent the effects of roughness and gravity on the drop's shape, water drops of $1\,\mu L$ were deposited on at least five different spots of the substrates. The drop contour was analyzed from the image of the deposited liquid drop on the surface, and the contact angle was determined using the Young–Laplace fitting method.[58,59] To reduce errors due to roughness and heterogeneity, the average contact angle values were measured about 15 s after the deposition. All measurements were carried out at $22\,°C$ and ambient humidity.

3. Results and Discussion

In this research, LST was successfully employed to modify the surface properties of 3D-printed Ir-PLA samples, to enhance corrosion resistance and mechanical performance in saline environments. **Figure 3** shows an image of the surface of 3D Ir-PLA after the LST process. **Table 4** summarizes the experimental
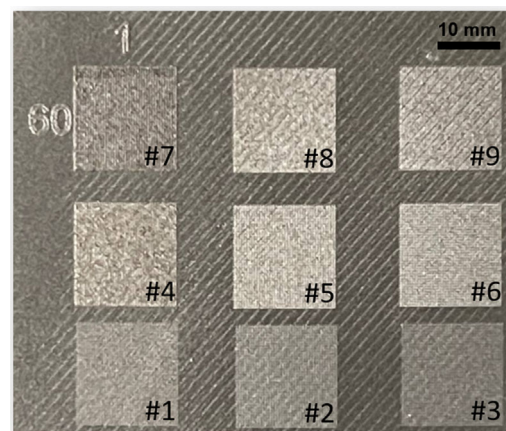
Figure 3. Actual photograph from the 3D Ir-PLA samples after applying LST process with 40–60 W laser power and 1.2–6 mm s^{-1} scanning speed.

parameters used for LST and the resulting surface characteristics for the nine samples tested. The interplay of these parameters also impacted the contact angle, a key indicator of surface wettability and potential corrosion susceptibility.

3.1. Width of Laser Track

The statistical analysis for the width of the laser track, as presented in the ANOVA **Table 5**, revealed that the variation observed might be primarily attributed to factors beyond the current model's scope. The individual model terms were also found to be statistically insignificant, suggesting that the relationship between the LST parameters and the width of the laser track may not be adequately captured by the current model. The results highlight the potential for further exploration and model refinement to gain a more comprehensive understanding of the factors influencing the width of the laser track during LST of Ir-PLA.

Equation (4) presents a regression equation of the width of laser track and its relationship with two main factors where A represents laser power and B represents scanning speed.

Table 4. Summary of all results in this study.

| Sample	Inputs		Outputs		
	Laser power [w]	Scanning speed [mm s^{-1}]	Width of laser track [μm]	Roughness, Ra [μm]	Contact angle [°]
#1	40	1.2	50 ± 1.26	3.18 ± 0.07	45 ± 1.08
#2	40	3.6	48 ± 1.11	2.53 ± 0.06	50 ± 1.21
#3	40	6	45 ± 1.31	2.01 ± 0.04	55 ± 1.32
#4	50	1.2	49 ± 1.16	3.26 ± 0.07	43 ± 1.03
#5	50	3.6	46 ± 1.15	2.81 ± 0.06	48 ± 1.15
#6	50	6	44 ± 1.3	2.22 ± 0.05	52 ± 1.24
#7	60	1.2	50 ± 1.2	2.47 ± 0.06	40 ± 0.96
#8	60	3.6	48 ± 1.15	2.01 ± 0.04	45 ± 1.08
#9	60	6	51 ± 1.22	1.49 ± 0.03	50 ± 1.20
Reference sample			–	0.7 ± 0.02	57 ± 1.07

Table 5. ANOVA for the effects of laser power and scanning speed on width of laser track.

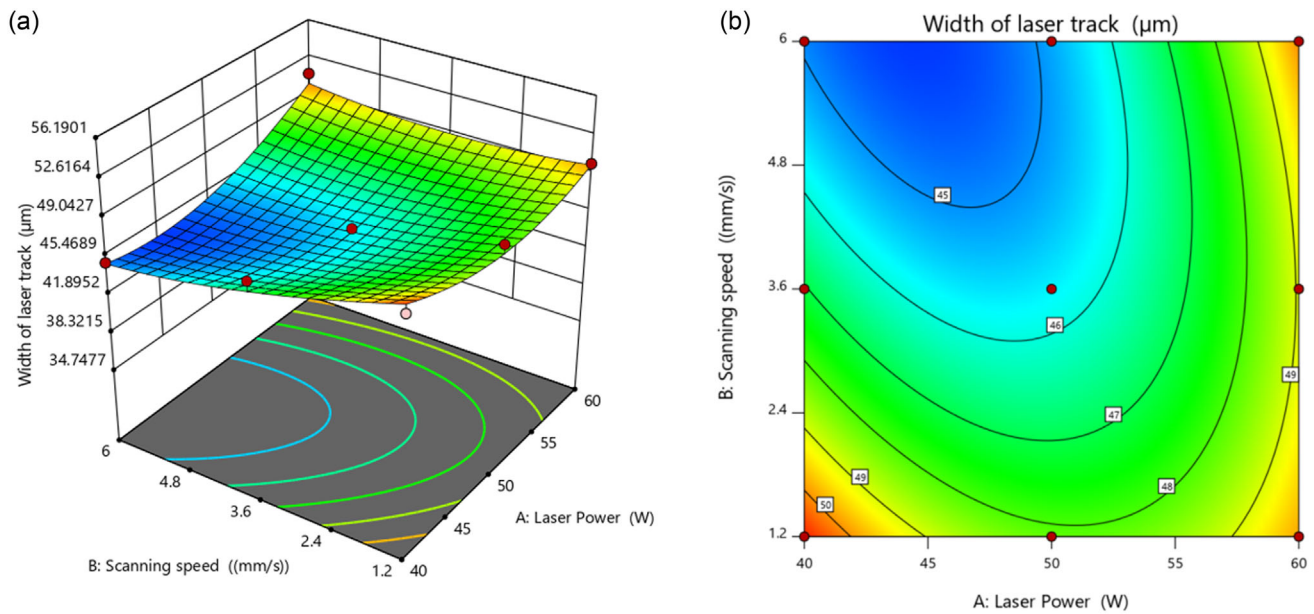| Source	Sum of squares	df	Mean square	F-value	p-value
Model	1.88E + 09	5	3.75E + 08	4.1	0.1376
A—laser power	2.87E + 08	1	2.87E + 08	3.14	0.1747
B—scanning speed	5.74E + 08	1	5.74E + 08	6.27	0.0875
AB	4.31E + 08	1	4.31E + 08	4.71	0.1186
A^2	4.97E + 08	1	4.97E + 08	5.43	0.1021
B^2	8.70E + 07	1	8.70E + 07	0.9494	0.4017
Residual	2.75E + 08	3	9.16E + 07	–	–
Cor Total	2.15E + 09	8	–	–	–

$$(\text{Width of laser track})^3 = +95659.78 + 6921.00 \times A - 9781.50$$
$$\times B + 10381.50 \times AB + 15770.33$$
$$\times A^2 + 6594.83 \times B^2$$
$$(4)$$

Figure 4 demonstrates a visual analysis of the relationship between laser power, scanning speed, and the resulting width of the laser track in a surface texturing process. Two complementary plots (Figure 4a,b) are shown. Figure 4a, the "predicted versus actual" plot illustrates a positive correlation between the predicted and actual values for the cube of the width of the laser track. The points cluster around the diagonal line, indicating reasonable model accuracy, but with some scatter suggesting room for improvement. Figure 4b, the "perturbation" plot, reveals the impact of laser power (factor A) and scanning speed (factor B) on the width of the laser track. The curved lines for both factors indicate a nonlinear relationship, with laser power exhibiting a more significant impact on the width compared to scanning speed. The plot also highlights an optimal region around the reference point (50 W laser power, 3.6 mm s^{-1} scanning speed) for achieving narrower laser tracks. Overall, these plots provide valuable insights for optimizing LST processes by highlighting the complex interplay of laser power and scanning speed in determining track width.

Figure 5 offers a visual representation of the relationship between laser power, scanning speed, and the resulting width of the laser track in a surface texturing process. The 3D response surface plot and the contour plot work in tandem to illustrate the complex, nonlinear relationship between these parameters. The 3D plot provides a spatial understanding of how the predicted track width changes across different combinations of laser power and scanning speed, while the contour plot offers a simplified, top-down view with lines of equal track width. The elliptical
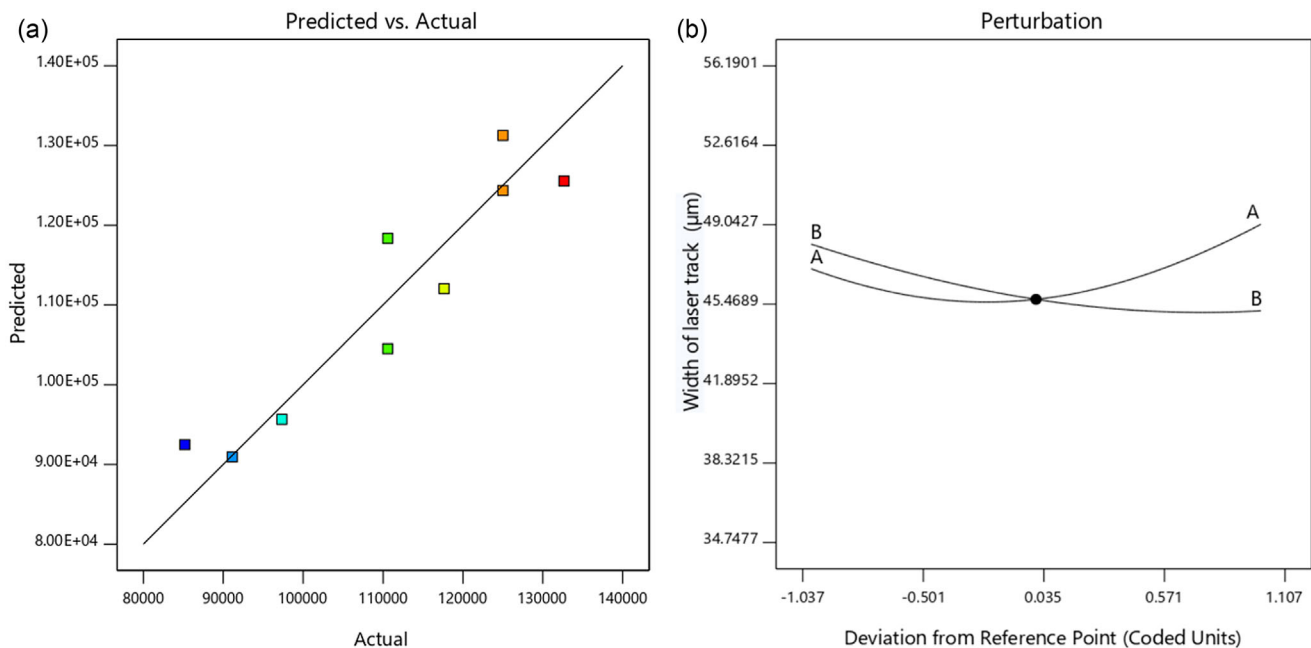
Figure 4. Analysis of the effects of laser power and scanning speed on width of laser track: a) predicted versus actual values and b) perturbation plots.

**ADVANCED
SCIENCE NEWS**

www.advancedsciencenews.com

**ADVANCED
ENGINEERING
MATERIALS**

www.aem-journal.com

Figure 5. a) 3D response surface. b) Contour plot for width of laser track.

pattern of the contours further emphasizes the nonlinear interaction between the two parameters, indicating that the effect of one parameter on track width is dependent on the level of the other. The plots reveal that increasing laser power generally leads to slightly narrower tracks, highlighting the importance of considering the combined effect of both parameters during optimization. The visualization also aids in identifying an optimal region, around 50 W laser power and 3.6 mm s^{-1} scanning speed, where relatively narrower laser tracks can be achieved.

Overall, these plots provide valuable insights for optimizing LST processes by highlighting the complex interplay of laser power and scanning speed in determining track width, which is crucial for achieving desired surface properties and functionalities in various applications.

Figure 6 showcases a series of microscopic images illustrating the effect of laser power (40, 50, 60 W) and scanning speed (1.2, 3.6, 6 mm s^{-1}) on the surface morphology of a textured material. Each image is labeled with a sample number (#1–9)
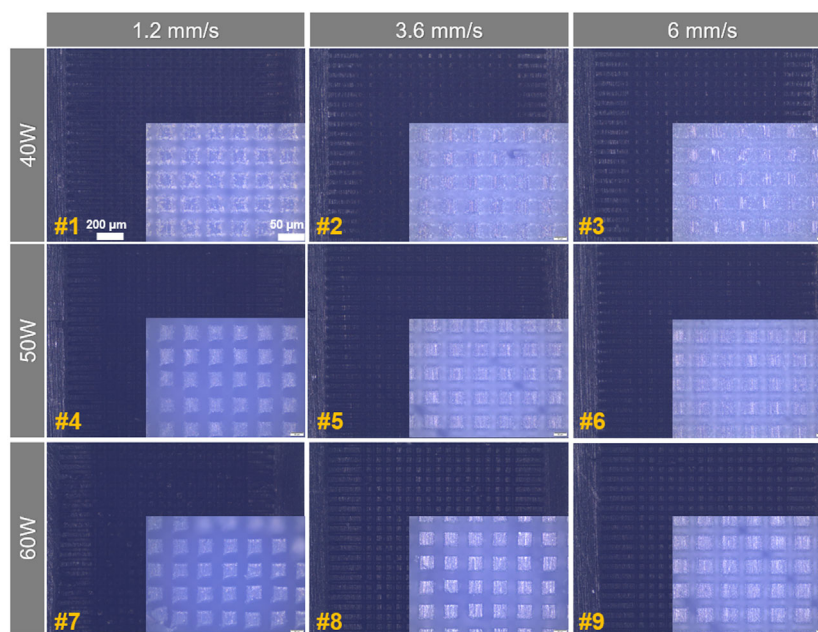
Figure 6. Microscopic images of the effect of laser power (40, 50, 60 W) and scanning speed (1.2, 3.6, 6 mm s^{-1}) on the surface morphology of a textured Ir-PLA.

and the scale bar indicates a 200 μm reference length. Both The corrosion susceptibility and limited mechanical properties of 3D printed Ir-PLA pose challenges to its application in demanding environments; particularly in marine settings, laser power and scanning speed play a significant role in the resulting surface texture. At lower power (40 W), the surface features are less pronounced, with shallower indentations and smoother areas. As the power increases, the texture becomes more defined, with deeper, more pronounced grooves and ridges. Scanning speed also impacts the texture: slower speeds (1.2 mm s^{-1}) result in denser patterns, while faster speeds (6 mm s^{-1}) create more widely spaced features. Overall, the images reveal the complex interplay between laser power and scanning speed in determining the final surface texture, highlighting the potential for fine-tuning these parameters to achieve desired surface properties.

3.2. Surface Roughness

In contrast to the width of the laser track, ANOVA for Ra yielded a statistically significant model (F-value = 235.77, p-value = 0.0004), as depicted in the corresponding ANOVA **Table 6**. This indicates that the model effectively explains a substantial portion of the observed variation in surface roughness. The analysis further identified laser power, scanning speed, and the quadratic term of laser power as significant model terms (p-values < 0.05), suggesting that these parameters have a considerable influence on the surface roughness of the laser-polished Ir-PLA samples. The negative coefficients associated with laser power and scanning speed in the ANOVA equation imply that increasing either of these parameters tends to decrease surface roughness. The negative coefficient for the quadratic term of laser power suggests a nonlinear relationship between laser power and surface roughness, indicating the existence of an optimal laser power level for achieving minimum roughness. The response surface plot and contour plot visually illustrate the combined effect of laser power and scanning speed on surface roughness, aiding in the identification of optimal process conditions.

Equation (5) provides a regression equation for surface roughness.
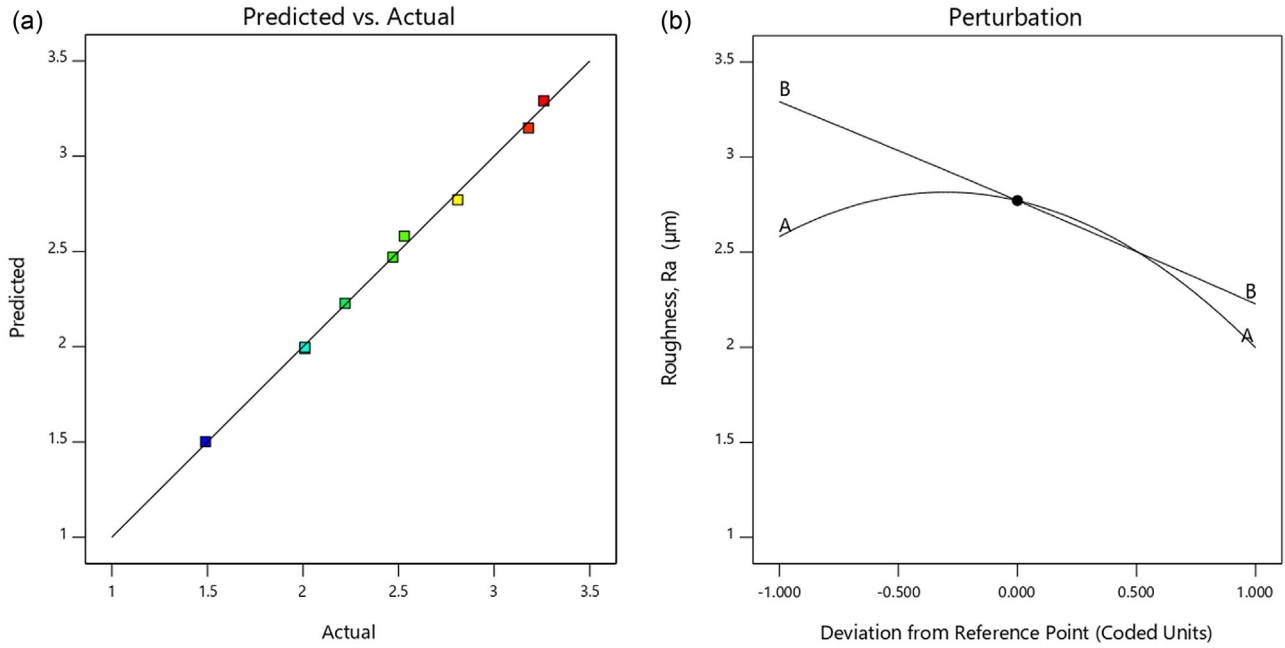
$$
\begin{aligned}
\text{Surface roughness, Ra} = {} & -6.68472 + 0.445375 \times A - 0.305903 \\
& \times B + 0.001979 \times AB - 0.004817 \\
& \times A^2 - 0.002025 \times B^2
\end{aligned}
$$

$$(5)$$

Figure 7 presents a visual analysis of the relationship between the predicted and actual values of Ra in an LST process, as well as the impact of laser power (factor A) and scanning speed (factor B) on Ra. The two plots, predicted versus actual (Figure 7a) and perturbation (Figure 7b), offer complementary insights into the model's accuracy and the influence of process parameters on surface roughness. The strong correlation between predicted and actual Ra values in plot (a) suggests that the model can be reliably used to guide process parameter selection. The perturbation plot (b) reveals the complex interplay between laser power and scanning speed, highlighting the need for careful optimization to achieve the desired surface roughness. The steeper slope for laser power in the perturbation plot indicates its greater influence on Ra compared to scanning speed within the tested range. The plot also shows that decreasing laser power initially leads to a rapid decrease in roughness, but the effect diminishes at higher power levels, while increasing scanning speed consistently reduces roughness, with the impact becoming less pronounced at higher speeds. The identification of an optimal region in the perturbation plot could help in selecting parameter combinations that minimize surface roughness while maintaining other desired properties of the textured surface.

Figure 8 provides a visual analysis of the relationship between laser power, scanning speed, and the resulting Ra in an LST process. The 3D response surface plot (Figure 8a) and the contour plot (Figure 8b) work together to illustrate the complex, nonlinear relationship between these parameters. The 3D plot offers a spatial understanding of how the predicted Ra changes across different combinations of laser power and scanning speed, revealing a general trend of decreasing Ra with increasing laser power, especially at lower scanning speeds. The contour plot, with its elliptical pattern of contour lines representing areas of equal Ra, further emphasizes the non-linear interaction between the two parameters and the varying sensitivity of Ra to changes in power and speed. The plots highlight the importance of considering the combined effect of both parameters during optimization, as the impact of changing one parameter on surface roughness depends on the level of the other. The visualization also aids in identifying an optimal region, around 50 W laser power and 3.6 mm s^{-1} scanning speed, where a combination of moderate laser power and scanning speed could lead to minimal surface roughness. Overall, these plots provide valuable insights for optimizing LST processes by highlighting the complex interplay of laser power and scanning speed in determining surface roughness, which is crucial for achieving desired surface properties and functionalities in various applications.

Figure 9 displays a series of 3D surface reconstructions of Ir-PLA samples that have undergone LST. Nine samples are presented, arranged in a grid where columns represent increasing scanning speeds (1.2, 3.6, 6 mm s^{-1}) and rows represent increasing laser power (40, 50, 60 W). The color gradient indicates the depth of the features, with red being the highest points and blue

Table 6. ANOVA for the effects of laser power and scanning speed on surface roughness.

Source	Sum of squares	df	Mean square	F-value	p-value
Model	2.68	5	0.5359	235.77	0.0004
A—laser power	0.5104	1	0.5104	224.54	0.0006
B—scanning speed	1.7	1	1.7	746.11	<0.0001
AB	0.009	1	0.009	3.97	0.1403
A^2	0.464	1	0.464	204.12	0.0007
B^2	0.0003	1	0.0003	0.1198	0.7521
Residual	0.0068	3	0.0023	–	–
Cor Total	2.69	8	–	–	–

**ADVANCED
SCIENCE NEWS**

www.advancedsciencenews.com

**ADVANCED
ENGINEERING
MATERIALS**

www.aem-journal.com

Figure 7. Analysis of the effects of laser power and scanning speed on surface roughness: a) predicted versus actual values and b) perturbation plots.
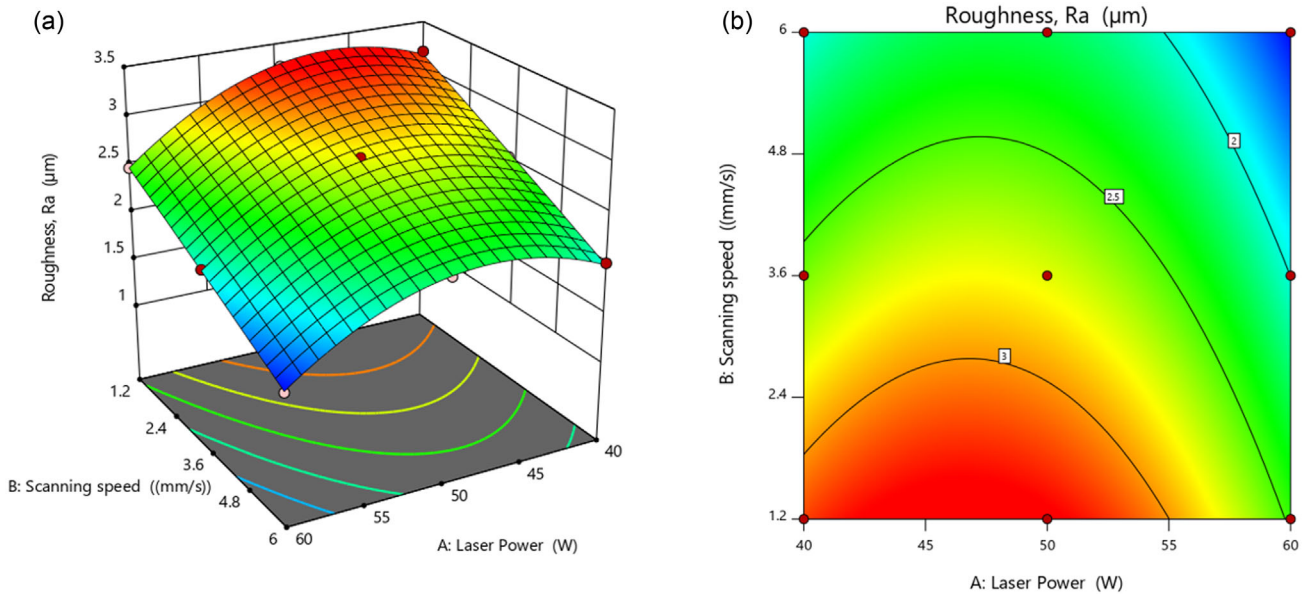
Figure 8. a) 3D response surface and b) contour plot for surface roughness after LST.

being the lowest points. As laser power increases (moving down the rows), the textured features become more pronounced, with deeper valleys and taller peaks. This indicates a greater removal of material at higher power levels. As scanning speed increases (moving across the columns), the distance between textured features increases. This suggests that at higher speeds, the laser has less time to interact with each point on the surface, resulting in wider spacing. The combined effect of laser power and scanning speed results in a variety of surface textures.

3.3. Contact Angle

The ANOVA for the contact angle also yielded a statistically significant model (F-value = 240.00, p-value = 0.0004), as shown in the corresponding ANOVA (**Table 7**). This implies that the model effectively captures the variation in contact angle observed in the laser-polished Ir-PLA samples. Laser power and scanning speed were identified as significant model terms (p-values < 0.05), while the interaction and quadratic terms were found to be
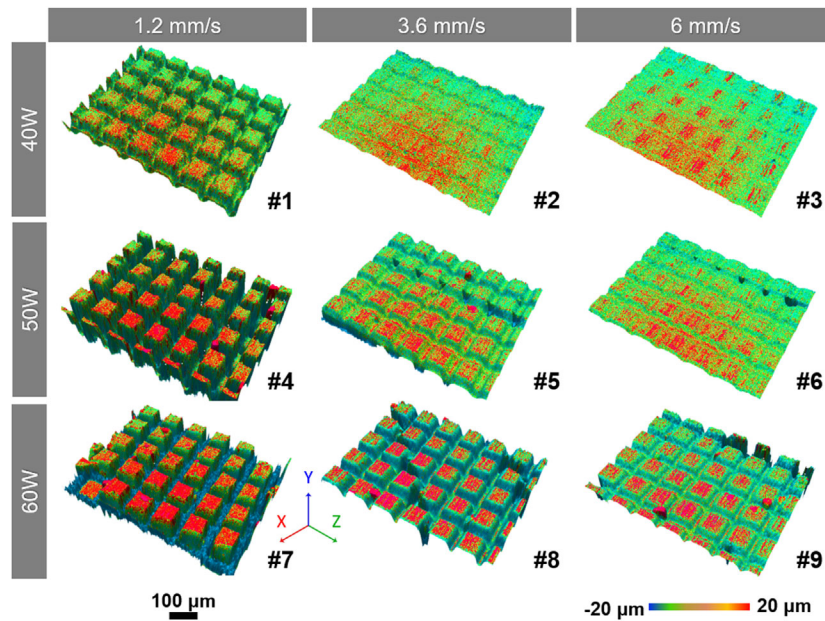
**ADVANCED
SCIENCE NEWS**

www.advancedsciencenews.com

**ADVANCED
ENGINEERING
MATERIALS**

www.aem-journal.com

Figure 9. 3D reconstruction of all samples of Ir-PLA samples after LST with different patterns.

Table 7. ANOVA for the effects of laser power and scanning speed on contact angle.

| Source	Sum of squares	df	Mean square	F-value	p-value
Model	177.78	5	35.56	240	0.0004
A—laser power	37.5	1	37.5	253.12	0.0005
B—scanning speed	140.17	1	140.17	946.12	<0.0001
AB	0	1	0	0	1
A^2	0.0556	1	0.0556	0.375	0.5836
B^2	0.0556	1	0.0556	0.375	0.5836
Residual	0.4444	3	0.1481	–	–
Cor Total	178.22	8	–	–	–

statistically insignificant. The negative coefficient for laser power suggests that an increase in laser power generally leads to a decrease in the contact angle. Conversely, the positive coefficient for scanning speed indicates that increasing the scanning speed tends to increase the contact angle. The absence of significant interaction and quadratic terms suggests a relatively straightforward relationship between laser power, scanning speed, and contact angle within the investigated parameter range. The response surface plot and contour plot visually depict the combined effect of laser power and scanning speed on the contact angle, facilitating the selection of appropriate process parameters to achieve a desired contact angle.

Equation (6) presents regression equation of contact angle

$$\text{Contact angle} = +48.48611 - 0.083333 \times A + 2.22222 \times B - 5.10687E - 17 \times AB - 0.001667 \times A^2 - 0.028935 \times B^2 \quad (6)$$

Figure 10 presents a visual analysis of the relationship between predicted and actual values of contact angle in a LST process, as well as the impact of laser power and scanning speed on the contact angle. The "predicted versus actual" plot (Figure 10a) demonstrates the high accuracy of the predictive model for contact angle, as the points cluster closely around the diagonal line, indicating a strong positive correlation between predicted and actual values. The "perturbation" plot (Figure 10b) reveals the relative importance and linear effects of laser power and scanning speed on the contact angle. The steeper slope for scanning speed suggests its greater influence on contact angle compared to laser power within the tested range. The plot also shows that increasing scanning speed leads to an increase in contact angle, while increasing laser power leads to a decrease. The black dot represents the reference point, indicating the predicted contact angle at the current settings for laser power and scanning speed. Overall, these plots provide valuable insights for optimizing the LST process, highlighting the model's accuracy and the interplay of laser power and scanning speed in achieving desired contact angles.

Figure 11 presents a visual analysis of the relationship between laser power, scanning speed, and the resulting contact angle in a surface texturing process. The 3D response surface plot (Figure 11a) and the contour plot (Figure 11b) work together to illustrate the straightforward, linear relationship between these parameters. The 3D plot offers a spatial understanding of how the predicted contact angle changes across different combinations of laser power and scanning speed, revealing a clear downward slope as laser power increases and an upward slope as scanning speed increases. The contour plot, with its parallel and evenly spaced contour lines representing areas of equal contact angle, further emphasizes the linear relationship and the absence of interaction between the two parameters. The plots show that increasing laser power consistently decreases the contact angle,
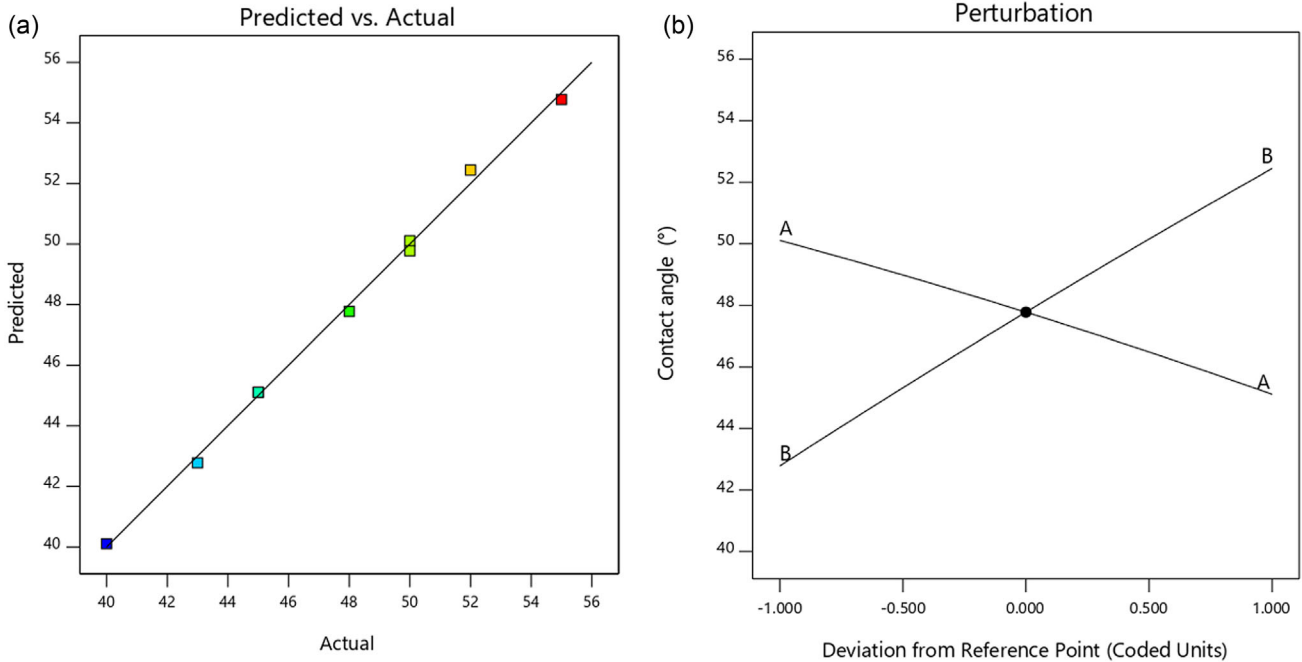
Figure 10. Analysis of the effects of laser power and scanning speed on contact angle: a) predicted versus actual values and b) perturbation plots.
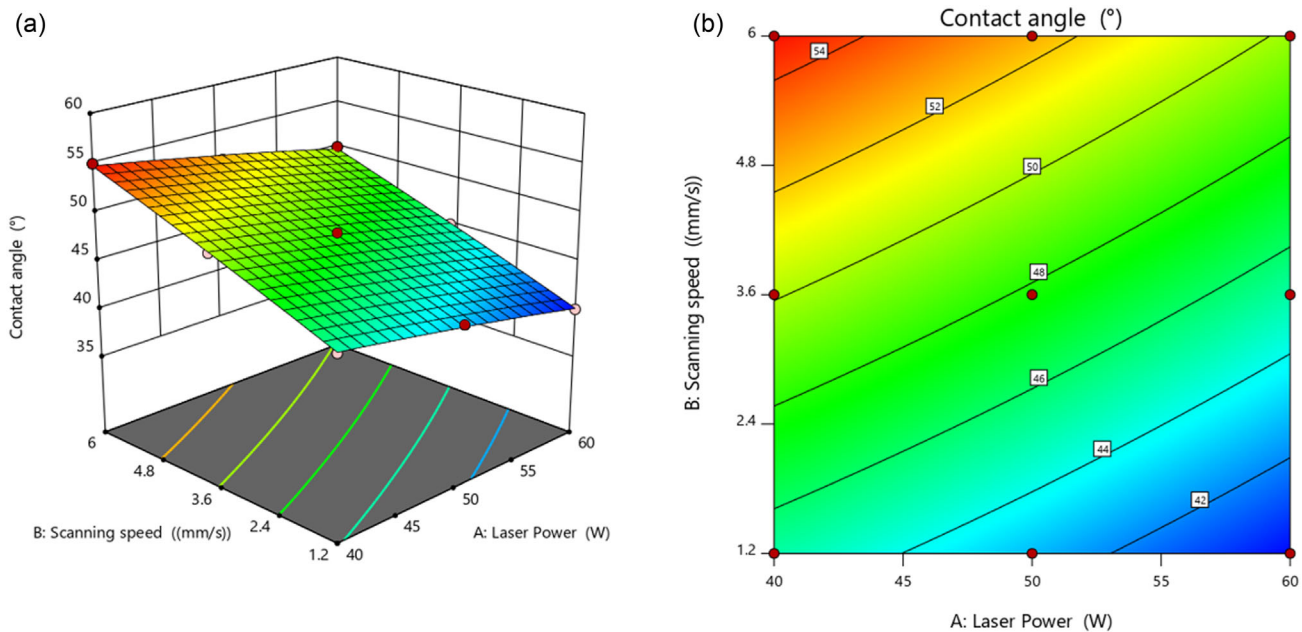

Figure 11. a) 3D response surface and b) contour plot for contact angle after LST.

while increasing scanning speed consistently increases it, allowing for predictable control over the contact angle by adjusting the laser parameters. Overall, these plots provide valuable insights for optimizing LST processes by highlighting the simple and predictable relationship between laser power, scanning speed, and contact angle, making it easier to select the appropriate parameters to achieve a desired contact angle for specific applications.

3.4. Tensile Test

The load-displacement curves provide in **Figure 12** compelling evidence of the positive impact of LST on the mechanical properties of Ir-PLA. The distinct difference in the behavior of the laser-treated material (pattern #9) compared to the untreated material underscores the efficacy of this technique.
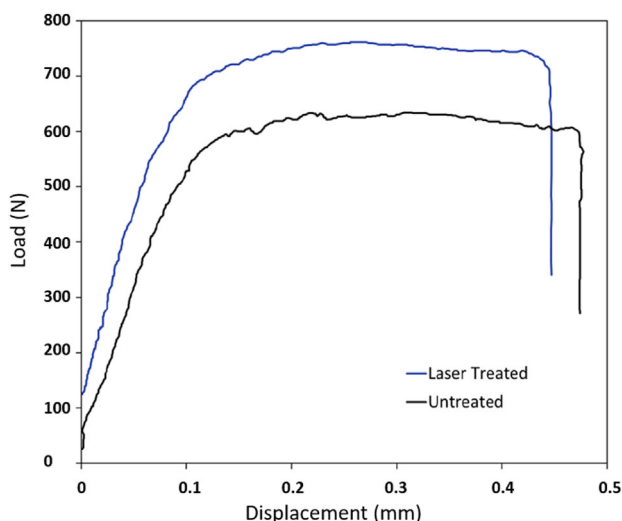
Figure 12. Load-displacement curves for untreated sample, black color, and laser-treated sample #9, blue color.

The laser-treated material exhibits a marked increase in both load-bearing capacity and ductility, signifying enhanced strength and toughness. This improvement can be attributed to the microstructural modifications and patterned surface texture induced by the laser treatment, which likely promotes better stress distribution, load transfer, and resistance to crack initiation and propagation. The observed enhancement in mechanical properties aligns with previous research on the LST of various materials. Studies have shown that laser treatment can induce surface hardening, grain refinement, and the formation of beneficial residual stresses, all of which contribute to improved mechanical performance. The creation of a patterned surface texture can further enhance these effects by providing additional sites for stress dissipation and promoting interlocking between the material and any applied coatings[60] or adhesives.

The present study's findings, particularly the significant increase in both strength and ductility, are particularly noteworthy. While previous work has demonstrated improvements in individual mechanical properties, the simultaneous enhancement of both strength and ductility is less common and highly desirable for many applications.[61–63] This suggests that the specific laser treatment parameters used in this study, resulting in pattern #9, were particularly effective in optimizing the material's microstructure and surface morphology for improved mechanical performance.

The increased strength and ductility could enable the material to withstand higher loads and more significant deformations without failure, making it suitable for structural components, impact-resistant parts, and other applications where mechanical reliability is critical. Furthermore, the improved toughness could extend the material's service life and reduce the risk of catastrophic failure, leading to enhanced safety and durability.

The data for sample #9 shows promising results that could justify its selection for further testing, such as tensile and corrosion tests. The roughness value (Ra) for sample #9 is 1.49 μm, which is the lowest among all the samples tested. Lower surface roughness is generally associated with improved corrosion resistance, as it reduces the available surface area for corrosive agents to attack and can also hinder the formation of localized corrosion sites. Additionally, lower roughness can lead to better mechanical properties, such as increased fatigue life and wear resistance. The contact angle for sample #9 is 50°. While not the highest in the dataset, it suggests a moderately hydrophobic surface, which can be beneficial in resisting the penetration of corrosive liquids. The combination of low roughness and moderate hydrophobicity could create a synergistic effect in enhancing corrosion resistance. The laser power (60 W) and scanning speed (6 mm s^{-1}) used for sample #9 are within the range of parameters explored in the study. This indicates that the favorable surface properties were achieved using practical and accessible processing conditions. The presence of a clear pattern in the surface texture of sample #9, as observed in the microscopic images, further supports its potential for enhanced performance. The pattern could provide additional benefits, such as improved adhesion or reduced friction, depending on the specific application.

Sample #9 exhibits a combination of low surface roughness, moderate hydrophobicity, and a patterned surface texture, all achieved using practical laser parameters. These characteristics suggest that this sample could exhibit superior corrosion resistance and mechanical properties compared to the other samples tested, making it a strong candidate for further evaluation through tensile and corrosion tests.

3.5. Corrosion Resistance

Figure 13 illustrates the corrosion resistance of Ir-PLA samples subjected to two different treatments. Figure 13a shows a sample treated with LST, while Figure 13b shows an untreated sample. Both samples were exposed to a corrosive environment, likely a saline solution, based on the context of the research article in Section 2.

As shown in Figure 13a, the laser-treated sample exhibits significantly less corrosion compared to the untreated sample. The surface appears relatively intact, with minimal signs of rust or degradation. This suggests that the LST process has effectively enhanced the corrosion resistance of the Ir-PLA. The patterned texture created by the laser treatment likely contributes to this improvement by altering the surface chemistry and morphology, potentially reducing the active surface area exposed to the corrosive medium and hindering the diffusion of corrosive species.

As shown in Figure 13b, in contrast, the untreated sample shows severe corrosion, with extensive rust formation covering most of the surface. This indicates that the untreated Ir-PLA is highly susceptible to corrosion in the given environment. The absence of any surface treatment leaves the material vulnerable to corrosive attack, leading to rapid degradation and loss of structural integrity.

Figure 14 presents a visual comparison of the corrosion resistance of 3D-printed Ir-PLA samples subjected to varying LST parameters after exposure to a corrosive saline environment. The samples are arranged in a grid, with columns representing different scanning speeds (1.2, 3.6, and 6 mm s^{-1}) and rows representing different laser powers (40, 50, and 60 W). An untreated reference sample (Ref.) is also included for comparison.
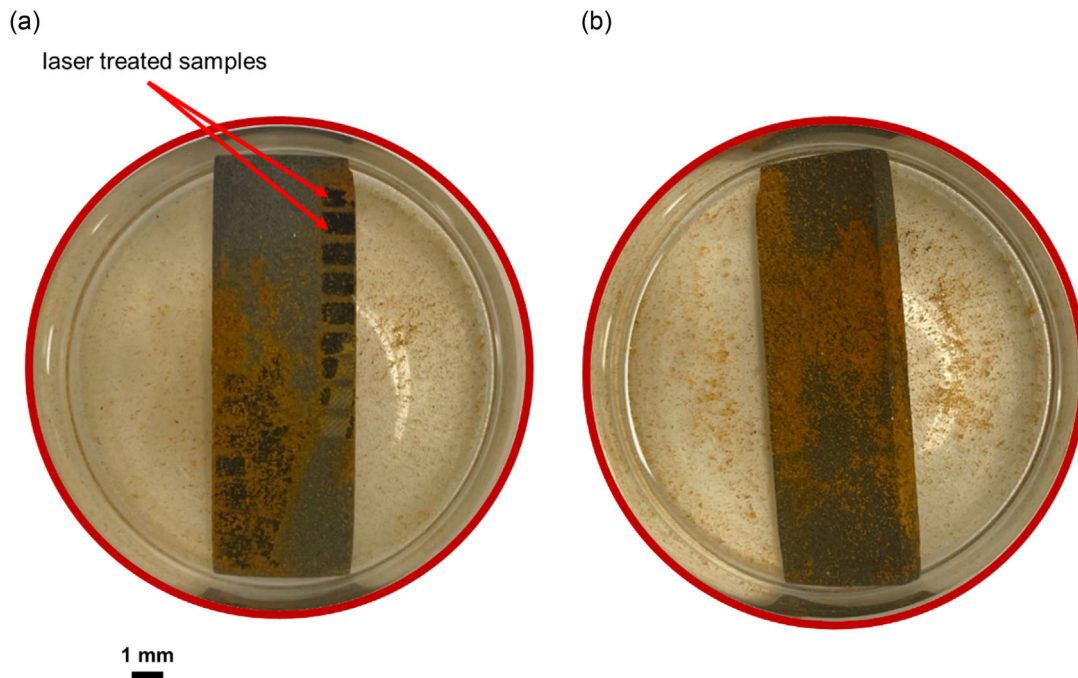
Figure 13. a) Laser-treated sample. b) Untreated sample after exposure to saline solution environment.
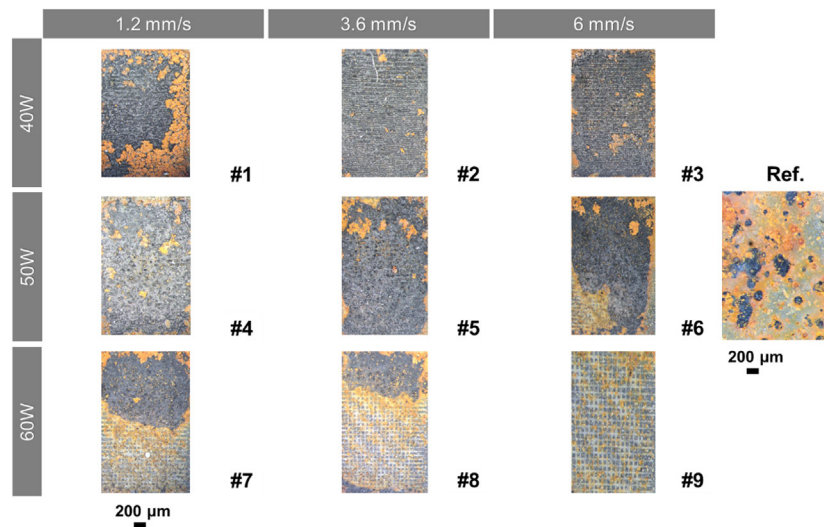
Figure 14. Optical images of the surface of all patterns in this study after 30 days of exposure to saline solution.

At 40 W laser power level, all samples exhibit significant corrosion, regardless of scanning speed. This suggests that 40 W is insufficient to induce surface modifications that effectively enhance corrosion resistance. Samples treated with 50 W laser power show varying degrees of corrosion depending on the scanning speed. The sample treated at $1.2 \, \text{mm s}^{-1}$ (#4) shows the most severe corrosion, while the sample treated at $6 \, \text{mm s}^{-1}$ (#6) shows the least. This indicates that higher scanning speeds might lead to better corrosion resistance at this power level. Samples treated with 60 W laser power demonstrate the highest overall corrosion resistance, with the sample treated at $6 \, \text{mm s}^{-1}$ (#9) showing the least corrosion. This suggests that a combination of high laser power and high scanning speed is most effective in enhancing corrosion resistance. The untreated sample exhibits the most severe corrosion, with extensive rust formation, indicating the necessity of LST for improving corrosion resistance in Ir-PLA.

Pattern #9, treated with 60 W laser power and $6 \, \text{mm s}^{-1}$ scanning speed, demonstrates superior corrosion resistance compared to other patterns for several reasons: The sample

shows the least amount of rust formation and surface degradation among all tested samples, indicating the highest level of protection against the corrosive environment. The combination of high laser power and high scanning speed likely creates a unique surface morphology with optimal roughness, wettability, and microstructure, which collectively contribute to enhanced corrosion resistance. The consistent and well-defined pattern observed in sample #9 suggests that the LST process can be reliably reproduced to achieve similar results.

Based on these observations, pattern #9 stands out as the most promising candidate for further investigation and potential implementation in applications requiring enhanced corrosion resistance for 3D-printed Ir-PLA components in saline environments.

Wettability plays a critical role in determining the corrosion resistance of materials, particularly in environments with high moisture or exposure to corrosive agents, such as marine settings.[64] Wettability is typically assessed through the measurement of the contact angle between a water droplet and the material's surface. A higher contact angle indicates a more hydrophobic (water-repellent) surface, while a lower contact angle suggests a hydrophilic surface, which readily absorbs or interacts with water.

In this study, the LST process significantly altered the wettability of 3D-printed Ir-PLA by modifying the surface roughness and morphology. These changes in surface properties were reflected in the measured contact angles across different laser-treated samples. The untreated Ir-PLA surface exhibited a moderate contact angle, indicating a relatively hydrophilic nature that would allow water and corrosive agents, such as chloride ions in saline environments, to easily spread across and penetrate the material. This increases the likelihood of localized corrosion, particularly where the iron particles within the PLA matrix are exposed. However, the application of LST increased the surface roughness and created micro- and nanoscale patterns, which significantly impacted the wettability. The textured surfaces exhibited higher contact angles, especially for samples treated with higher laser power and scanning speed. For instance, sample #9, which was treated with 60 W laser power and 6 mm s⁻¹ scanning speed, displayed a contact angle of 50°, indicating an enhanced hydrophobic surface. This increase in hydrophobicity can be attributed to the laser-induced patterns that trap air pockets at the surface, reducing the actual contact area between the water and the material. As a result, the water forms droplets that are less likely to spread across the surface, reducing the material's exposure to corrosive agents.[65] The improvement in corrosion resistance due to increased hydrophobicity is supported by the visual and quantitative analysis of the corrosion tests.

Samples with higher contact angles showed significantly less surface degradation and rust formation after immersion in saline solutions. The reduced wettability hinders the ability of chloride ions and moisture to remain in prolonged contact with the material, thereby limiting the initiation and progression of corrosion.

In addition to influencing corrosion resistance, the laser-induced texturing also alters the mechanical properties of the surface. By optimizing the laser power and scanning speed, it is possible to tailor the surface roughness and, consequently, the contact angle to achieve a balance between mechanical strength and corrosion resistance. The combination of a more hydrophobic surface and improved structural integrity makes LST-treated Ir-PLA a promising material for use in environments where moisture and corrosive elements are prevalent.

4. Optimization

The optimization process aimed to identify the optimal laser power and scanning speed settings within specified ranges to achieve desired outcomes for width of laser track, Ra, and contact angle. The goal for the width of the laser track was to keep it within a specified range, while the roughness was to be minimized and the contact angle targeted at 47.5°. Six solutions were found, with solution #1 being selected as the optimal solution due to its highest desirability score of 0.923. This solution suggests using a laser power of 60.000 W and a scanning speed of 4.807 mm s⁻¹ to achieve a width of laser track of 49.368, roughness of 1.751, and a contact angle of 47.500. It is important to note that the other five solutions had significantly lower desirability scores, indicating they were less optimal in meeting the specified goals.

Table 8 outlines the constraints and goals for optimizing the LST process. It defines the desired ranges or targets for key parameters (laser power and scanning speed) and responses (width of laser track, roughness, and contact angle), along with their relative importance. The goal is to find the optimal combination of laser power and scanning speed that results in a laser track width within a specified range, minimizes surface roughness, and achieves a target contact angle of 47.5°. All factors are considered equally important in the optimization, and deviations from the target or range in either direction are equally undesirable.

Table 9 presents the results of an optimization process aimed at finding the best combination of laser power and scanning speed to achieve desired outcomes for the width of the laser track, Ra, and contact angle. Table 9 lists six potential solutions, each with a different combination of laser power and scanning

Table 8. Constraints and goals for optimizing the LST.

Name	Goal	Lower limit	Upper limit	Lower weight	Upper weight	Importance
A: laser power	is in range	40	60	1	1	3
B: scanning speed	is in range	1.2	6	1	1	3
Width of laser track	is in range	85 184	132 651	1	1	3
Roughness, Ra	minimize	1.49	3.26	1	1	3
Contact angle	is target = 47.5	40	55	1	1	3

**ADVANCED
SCIENCE NEWS**

www.advancedsciencenews.com

**ADVANCED
ENGINEERING
MATERIALS**

www.aem-journal.com

Table 9. Optimal solutions and desirability for laser power and scanning speed to maximize width of laser track, surface roughness, and contact angle in this study.

Number	Laser power	Scanning speed	Width of laser track	Roughness, Ra	Contact angle	Desirability	
1	60.000	4.807	49.368	1.751	47.500	0.923	Selected
2	60.000	4.942	49.427	1.723	47.762	0.915	–
3	40.000	3.396	47.366	2.630	49.700	0.501	–
4	40.000	3.349	47.429	2.642	49.604	0.501	–
5	40.000	3.449	47.297	2.618	49.806	0.501	–
6	40.000	3.466	47.274	2.613	49.841	0.501	–

speed, and the resulting predicted values for the width of the laser track, roughness, and contact angle. The desirability score, ranging from 0 to 1, indicates how well each solution satisfies the defined goals.

The solution labeled "Selected" (Number 1) has the highest desirability score (0.923), suggesting it is the optimal solution based on the specified constraints and goals. This solution recommends using a laser power of 60 W and a scanning speed of 4.807 mm s^{-1}. The other solutions have lower desirability scores, indicating they are less optimal in meeting the desired outcomes.

Figure 15 is an overlay plot that shows the optimal region for laser power (A) and scanning speed (B) to achieve specific goals for Ra, contact angle, and width of the laser track. The yellow-shaded area represents the region where all three goals are met. The points within the yellow area represent different combinations of laser power and scanning speed that meet the desired criteria. The optimal settings, indicated by the point within the yellow region closest to the target values for all three
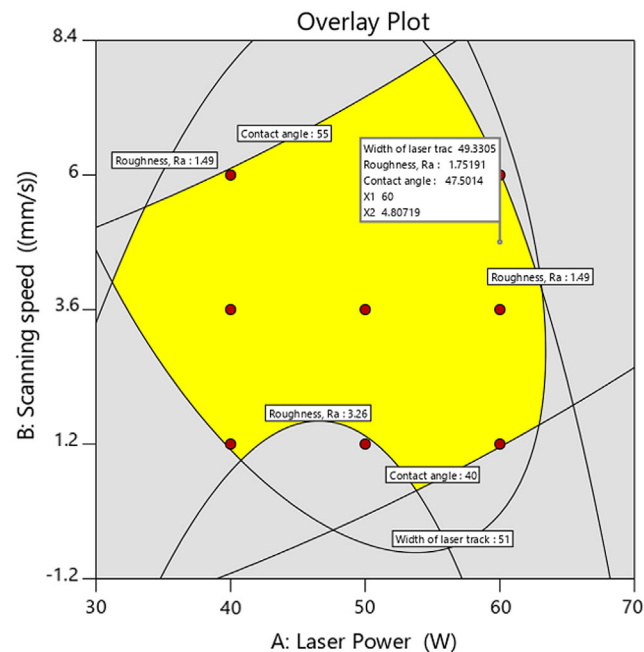
Figure 15. Overlay Plot for optimal laser power (A) and scanning speed (B) to achieve specific laser track width, surface roughness and contact angle goals.

responses, are ≈60 W laser power and 4.8 mm s^{-1} scanning speed. The plot also shows the individual desirability functions for each response, indicated by the diagonal lines for contact angle and width of the laser track, and the curved lines for roughness. The desirability function for roughness indicates that lower roughness is more desirable, while the desirability functions for contact angle and width of the laser track indicate that values closer to the target values (47.5° and unspecified, respectively) are more desirable.

When considering surface treatment methods for enhancing corrosion resistance and mechanical strength, several approaches are available, including chemical coatings, mechanical abrasion, and LST. Chemical coatings, such as anticorrosion paints or electroplated layers, can offer effective corrosion protection at relatively low upfront costs. However, these coatings often require periodic reapplication, especially in harsh environments like marine settings, which increases long-term maintenance costs. Additionally, the adhesion of such coatings on 3D-printed composites may not be as strong as on metals, potentially leading to premature failure in high-stress applications. Mechanical abrasion methods, such as sandblasting, can improve surface roughness and adhesion for coatings but may lead to material loss, especially in delicate 3D-printed structures. Abrasive techniques also lack the precision needed to optimize surface patterns for specific performance metrics like wettability or mechanical strength.

In contrast, LST provides a highly efficient, one-time surface modification technique that directly alters the material's surface properties without the need for additional layers or material loss. While the initial equipment and operational costs of LST are higher compared to chemical coatings or mechanical abrasion, the long-term benefits, including enhanced durability, lower maintenance, and extended component life, can offset the upfront investment. LST's precision also allows for tailored surface features that optimize both corrosion resistance and mechanical properties, making it particularly advantageous for 3D-printed components with complex geometries.[50] Additionally, the integration of LST into the additive manufacturing process can streamline production, reducing time and material waste compared to more traditional surface treatments.

5. Remarks and Recommendations

The selection of 3D printing parameters, including nozzle temperature, print speed, and extrusion width, was carefully made to

ensure proper adhesion of iron particles within the PLA matrix and to maintain the structural and surface integrity of the printed samples. These parameters were chosen to minimize surface defects that could promote corrosion initiation. However, future studies will explore the effect of varying these parameters on the microscopic morphology of the material and its subsequent impact on corrosion performance. A systematic study on how changes in printing speed, temperature, and layer thickness influence surface roughness, porosity, and the material's resistance to corrosion will provide valuable insights into optimizing 3D-printed Ir-PLA composites for various environmental applications.

While visual observation of surface corrosion is a widely accepted method for comparing corrosion behavior, it has certain limitations, particularly in detecting internal or subsurface corrosion. Future studies will integrate additional quantifiable methods, such as weight loss measurements, electrochemical impedance spectroscopy (EIS), and potentiodynamic polarization. These techniques will provide more comprehensive data on corrosion resistance by allowing the assessment of material degradation both on the surface and internally. Such methods are essential for offering a more accurate evaluation of corrosion performance in 3D-printed Ir-PLA composites. Future research could explore several avenues to further enhance the performance of 3D-printed Ir-PLA composites treated with LST. One potential direction is to investigate the effects of different laser texturing patterns on both mechanical strength and corrosion resistance. While this study focused on specific patterns, other geometries—such as hierarchical or more complex micro/nanoscale patterns—may yield additional improvements in surface properties. Another promising area for exploration is the combination of LST with other surface treatments. For instance, applying chemical coatings or electroplating after LST could further enhance corrosion protection by leveraging the textured surface for better coating adhesion. Similarly, combining LST with heat treatment[66] or plasma treatment might result in even more significant improvements in mechanical strength and resistance to environmental degradation. Additionally, expanding the study to include other 3D-printed composite materials with different metal or polymer matrices would provide insights into the broader applicability of LST across various industries. Investigating the long-term performance of LST-treated components in real-world marine environments would also help validate the durability and reliability of the treatment.

6. Conclusions

In this study, we aim to determine the optimal input parameters, specifically laser power and scanning speed, for performing LST on Ir-PLA sheets to enhance their mechanical properties and corrosion resistance in saline solution. To minimize the number of tests and optimize the process, we employed response surface methodology for experimental design. The study examined several experimental responses, including laser track width, surface roughness (Ra), and contact angle. The main findings of this research can be listed as follows: 1) LST has been successfully demonstrated as an effective method for enhancing the corrosion

resistance and mechanical properties of 3D-printed Ir-PLA for saline applications. The process allows for controlled modification of surface roughness and wettability, leading to improved performance in corrosive environments. 2) The study identified an optimal combination of laser power and scanning speed ($60\,W$, $4.807\,mm\,s^{-1}$) that resulted in the most desirable surface characteristics and mechanical behavior. This highlights the importance of careful parameter selection in LST to achieve the desired outcomes. 3) The laser-treated samples exhibited significantly improved corrosion resistance compared to untreated samples, as evidenced by the reduced rust formation and surface degradation observed in the images. LST improved corrosion resistance by 80% and this suggests the potential for extending the service life of Ir-PLA components in corrosive environments through LST. 4) The load-displacement curves demonstrated a substantial increase in both strength and ductility of the laser-treated material, indicating improved mechanical performance. This enhancement can be attributed to the microstructural modifications and patterned surface texture induced by the laser treatment. 5) The findings of this study contribute to the growing body of knowledge on LST and its potential for enhancing the properties of 3D printed materials. The ability to tailor surface characteristics and mechanical behavior through laser processing opens up new possibilities for the use of Ir-PLA in various applications, particularly those requiring enhanced corrosion resistance and mechanical performance.

Conflict of Interest

The authors declare no conflict of interest.

Author Contributions

Mohammad Rezayat: conceptualization (supporting); data curation (equal); formal analysis (equal); investigation (equal); methodology (equal); software (lead); validation (lead); writing—original draft (lead); writing—review & editing (equal). **Mojtaba Karamimoghadam**: conceptualization (supporting); data curation (lead); formal analysis (equal); investigation (supporting); methodology (supporting); writing—original draft (supporting); writing—review & editing (supporting). **Mohammadreza Lalegani Dezaki**: data curation (supporting); investigation (equal); software (supporting); writing—review & editing (supporting). **Ali Zolfagharian**: formal analysis (supporting); investigation (supporting); methodology (equal); writing—review & editing (supporting). **Giuseppe Casalino**: formal analysis (supporting); investigation (supporting); methodology (supporting); writing—review & editing (supporting). **Antonio Mateo**: formal analysis (supporting); investigation (supporting); methodology (supporting); writing—review & editing (supporting). **Mahdi Bodaghi**: conceptualization (lead); formal analysis (lead); funding acquisition (supporting); investigation (lead); methodology (lead); supervision (lead); writing—original draft (supporting); writing—review & editing (lead).

Data Availability Statement

The data that support the findings of this study are available from the corresponding author upon reasonable request.

[1] M. Morcillo, B. Chico, L. Mariaca, E. Otero, *Corros. Sci.* **2000**, *42*, 91.

[2] D. A. Shifler, *Corros. Sci.* **2005**, *47*, 2335.

[3] M. Otieno, M. Thomas, *Marine Concrete Structures*, Elsevier, Kidlington, **2016**, pp. 171–196.

[4] E. Y. Salawu, O. O. Awoyemi, O. E. Akerekan, S. A. Afolalu, J. F. Kayode, S. O. Ongbali, I. Airewa, B. M. Edun, *E3S Web Conf.* **2023**, *430*, 01226.

[5] M. Wajahat, A. Z. Kouzani, S. Y. Khoo, M. A. P. Mahmud, *Adv. Eng. Mater.* **2024**, *26*, 2400199.

[6] M. Zeynivandnejad, M. Moradi, A. Sadeghi, *J. Manuf. Processes* **2023**, *101*, 234.

[7] J. S. Mohammed, *Methods Oceanogr.* **2016**, *17*, 97.

[8] R. K. Upadhyay, A. K. Mishra, A. Kumar, *Surf. Interfaces* **2020**, *21*, 100778.

[9] A. Bandyopadhyay, B. Heer, *Mater. Sci. Eng.: R: Rep.* **2018**, *129*, 1.

[10] Y. Tao, F. Kong, Z. Li, J. Zhang, X. Zhao, Q. Yin, D. Xing, P. Li, *J. Mater. Res. Technol.* **2021**, *15*, 4860.

[11] L. Zhou, J. Miller, J. Vezza, M. Mayster, M. Raffay, Q. Justice, Z. Al Tamimi, G. Hansotte, L. D. Sunkara, J. Bernat, *Sensors* **2024**, *24*, 2668.

[12] Y. Xu, F. Zhang, W. Zhai, S. Cheng, J. Li, Y. Wang, *Polymers* **2022**, *14*, 566.

[13] M. Bai, T. Liu, B. Liu, Y. Li, H. Yu, Y. Zhao, C. Yang, L. Song, W. Liu, *Surf. Coat. Technol.* **2024**, *489*, 131128.

[14] O. Menezes, T. Roberts, G. Motta, M.-H. Patrenos, W. McCurdy, A. Alotaibi, M. Vanderpool, M. Vaseghi, A. Beheshti, K. Davami, *Polym. Degrad. Stab.* **2022**, *199*, 109903.

[15] E. H. Tümer, H. Y. Erbil, *Coatings* **2021**, *11*, 390.

[16] T. M. Joseph, A. Kallingal, A. M. Suresh, D. K. Mahapatra, M. S. Hasanin, J. Haponiuk, S. Thomas, *Int. J. Adv. Manuf. Technol.* **2023**, *125*, 1015.

[17] M. Moradi, M. Rezayat, F. A. R. Rozhbiany, S. Meiabadi, G. Casalino, M. Shamsborhan, A. Bijoy, S. Chakkingal, M. Lawrence, N. Mohammed, M. Karamimoghadam, *Machines* **2023**, *11*, 950.

[18] M. Moradi, M. Karamimoghadam, S. Meiabadi, G. Casalino, M. Ghaleeh, B. Baby, H. Ganapathi, J. Jose, M. S. Abdulla, P. Tallon, M. Shamsborhan, M. Rezayat, S. Paul, D. Khodadad, *Mathematics* **2023**, *11*, 3022.

[19] M. Moradi, M. Karami Moghadam, M. Shamsborhan, M. Bodaghi, *J. Compos. Sci.* **2020**, *4*, 17.

[20] A. Shahrjerdi, M. Karamimoghadam, M. Bodaghi, *J. Compos. Sci.* **2023**, *7*, 151.

[21] D. Jiang, F. Ning, Y. Wang, *J. Mater. Process. Technol.* **2021**, *289*, 116952.

[22] R. T. Mushtaq, Y. Wang, C. Bao, X. Chen, S. Anwar, S. Sharma, A. M. Khan, K. Sharma, Y. S. Bisht, M. Abbas, D. Kozak, V. Tropša, *J. Mater. Res. Technol.* **2024**, *29*, 3168.

[23] H. Alzyod, J. Takacs, P. Ficzere, *J. Reinf. Plast. Compos.* **2023**, *43*, https://doi.org/10.1177/07316844231173059.

[24] H. Chen, H. Cui, Z. He, L. Lu, Y. Huang, *Mater. Chem. Phys.* **2021**, *259*, 123971.

[25] V. Kumar, S. K. Tiwari, N. Sharma, *Mater. Today Commun.* **2023**, *34*, 105184.

[26] A. Ronen, I. Etsion, Y. Kligerman, *Tribol. Trans.* **2001**, *44*, 359.

[27] J. A. Wahab, M. J. Ghazali, W. M. W. Yusoff, Z. Sajuri, *Trans. IMF* **2016**, *94*, 193.

[28] S. Pradhan, I. Shivakoti, G. Kibria, A. Sharma, M. Sekh, *AIP Conf. Proc.* **2023**, *2786*, 020010.

[29] M. Rezayat, H. Besharatloo, A. Mateo, *Metals* **2023**, *13*, 2021.

[30] M. Rezayat, M. Moradi, A. Mateo, *Int. J. Adv. Manuf. Technol.* **2024**, *132*, 4753.

[31] A. Cholkar, S. Chatterjee, S. Kumar, M. Sedaček, B. Podgornik, D. Kinahan, D. Brabazon, *Adv. Eng. Mater.* **2024**, *26*, 2401183.

[32] J. Zhang, D. Yang, A. Rosenkranz, J. Zhang, L. Zhao, C. Song, Y. Yan, T. Sun, *Adv. Eng. Mater.* **2019**, *21*, 1801016.

[33] J. Kechagias, D. Chaidas, N. Vidakis, K. Salonitis, N. M. Vaxevanidis, *Mater. Manuf. Processes* **2022**, *37*, 963.

[34] J. Xu, L. Zhou, G. Ma, G. Li, H. Zhao, H. Wang, *J. Mater. Res. Technol.* **2024**, *31*, 606.

[35] M. Morales, M. Rezayat, A. Mateo, *J. Energy Storage* **2024**, *78*, 110053.

[36] M. Rezayat, M. Morales, M. Moradi, A. Mateo, *Opt. Laser Technol.* **2024**, *171*, 110375.

[37] J. Xu, L. Chang, T. Chen, T. Ren, Y. Zhang, Z. Cai, *Compos. Struct.* **2023**, *322*, 117369.

[38] S. Costil, A. Lamraoui, C. Langlade, O. Heintz, R. Oltra, *Appl. Surf. Sci.* **2014**, *288*, 542.

[39] A. F. Obilor, M. Pacella, A. Wilson, V. V. Silberschmidt, *Int. J. Adv. Manuf. Technol.* **2022**, *120*, 103.

[40] D. Moskal, J. Martan, M. Honner, *Micromachines* **2023**, *14*, 1241.

[41] D. Song, X. Chen, M. Wang, Z. Wu, X. Xiao, *Chem. Eng. J.* **2023**, *474*, 146011.

[42] X. He, Q. Weng, R. Guo, L. Zhang, X. Sheng, D. Xie, *J. Mater. Sci. Technol.* **2024**, *201*, 197.

[43] V. Vijay Kumar, D. Narayanan, S. Chandran, S. Rajendran, S. Ramakrishna, *Lightweight and Sustainable Composite Materials*, Elsevier, Kidlington, **2023**, pp. 19–46.

[44] Y. Zhang, Z. Huang, H. Wang, J. Li, *ACS Appl. Mater. Interfaces* **2023**, *15*, 32984.

[45] Y. Zhang, Z. Wang, S. Huang, H. Liu, Y. Yan, *Corros. Sci.* **2024**, *235*, 112185.

[46] E. Ghassemieh, *New Trends and Developments in Automotive Industry*, InTech, New York, **2011**.

[47] M. Rezayat, M. Moradi, A. Mateo, *Int. J. Adv. Manuf. Technol.* **2023**, *128*, 3025.

[48] I. Singh, S. M. George, A. Tiwari, J. Ramkumar, K. Balani, *J. Mater. Res.* **2021**, *36*, 3985.

[49] R. T. Mushtaq, Y. Wang, C. Bao, M. Rehman, S. Sharma, A. M. Khan, E. M.-T. Eldin, M. Abbas, *Int. J. Biol. Macromol.* **2024**, *259*, 129201.

[50] A. Chalgham, A. Ehrmann, I. Wickenkamp, *Polymers* **2021**, *13*, 1239.

[51] J. Fournier, P. Ballard, P. Merrien, J. Barralis, L. Castex, R. Fabbro, *J. Phys. III* **1991**, *1*, 1467.

[52] N. Huda Abdul Razak, N. Amin, K. Sajedur Rahman, J. Pasupuleti, M. Akhtaruzzaman, K. Sopian, M. D. Albaqami, A. Mohamed Tighezza, Z. A. Alothman, M. Sillanpää, *Results Phys.* **2023**, *48*, 106435.

[53] J. Finger, B. Bornschlegel, M. Reininghaus, A. Dohrn, M. Nießen, A. Gillner, R. Poprawe, *Adv. Opt. Technol.* **2018**, *7*, 145.

[54] D. Min, J. Shen, S. Lai, J. Chen, N. Xu, H. Liu, *Opt. Lasers Eng.* **2011**, *49*, 89.

[55] ASTM Standards, *Standard Test Method for Tensile Properties Of Plastics*, ASTM International, West Conshohocken, PA **2012**, https://doi.org/10.1520/D0638-03.

[56] G. W. Melenka, B. K. O. Cheung, J. S. Schofield, M. R. Dawson, J. P. Carey, *Compos. Struct.* **2016**, *153*, 866.

[57] ASTM Standards, *Standard Guide for Laboratory Immersion Corrosion Testing ASTM G31-21*, 2nd ed. ASTM International, West Conshohocken, PA **2021**.

[58] H. Liu, G. Cao, *Sci. Rep.* **2016**, *6*, 23936.

[59] H. Tang, X. Cheng, *Measurement* **2022**, *188*, 110379.

[60] B. Meng, J. Wang, M. Chen, S. Zhu, F. Wang, *Corros. Sci.* **2023**, *225*, 111591.

[61] C. Grabowik, K. Kalinowski, G. Ćwikła, I. Paprocka, P. Kogut, *MATEC Web Conf.* **2017**, *112*, 04017.

[62] N. Naveed, *Polymers* **2021**, *13*, 1487.

[63] G. Atakok, M. Kam, H. B. Koc, *J. Mater. Res. Technol.* **2022**, *18*, 1542.

[64] Y. Yuan, T. R. Lee, *Contact Angle and Wetting Properties* Springer Nature Switzerland **2013**, pp. 3–34, https://doi.org/10.1007/978-3-642-34243-1_1.

[65] X. Wang, A. Hassan, H. Boudaoud, F. Xue, Z. Zhou, X. Liu, *Adv. Compos. Hybrid Mater.* **2023**, *6*, 170.

[66] L. Shao, S. Zhang, L. Hu, Y. Wu, Y. Huang, P. Le, S. Dai, W. Li, N. Xue, F. Xu, L. Zhu, *Materials* **2024**, *17*, 2785.